

www.acsnano.org

Hybrid Amyloid—Chitin Nanofibrils for Magnetic and Catalytic Aerogels

Mohammad Peydayesh,* Enrico Boschi, Massimo Bagnani, Daniel Tay, Felix Donat, Hamed Almohammadi, Mingqin Li, Mattia Usuelli, Toni Shiroka, and Raffaele Mezzenga*



Cite This: ACS Nano 2024, 18, 6690-6701



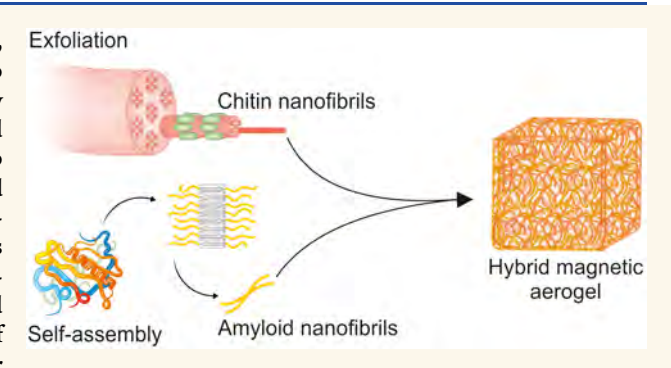
ACCESS

III Metrics & More

Article Recommendations

Supporting Information

ABSTRACT: In the quest for a sustainable and circular economy, it is essential to explore environmentally friendly alternatives to traditional petroleum-based materials. A promising pathway toward this goal lies in the leveraging of biopolymers derived from food waste, such as proteins and polysaccharides, to develop advanced sustainable materials. Here, we design versatile hybrid materials by hybridizing amyloid nanofibrils derived by self-assembly of whey, a dairy byproduct, with chitin nanofibrils exfoliated from the two distinct allomorphs of α -chitin and β -chitin, extracted from seafood waste. Various hydrogels and aerogels were developed via the hybridization and reassembly of these biopolymeric nanobuilding blocks, and they were further



magnetized upon biomineralization with iron nanoparticles. The pH-phase diagram highlights the significant role of electrostatic interactions in gel formation, between positively charged amyloid fibrils and negatively charged chitin nanofibrils. Hybrid magnetic aerogels exhibit a ferromagnetic response characterized by a low coercivity (<50 Oe) and a high specific magnetization (>40 emu/g) at all temperatures, making them particularly suitable for superparamagnetic applications. Additionally, these aerogels exhibit a distinct magnetic transition, featuring a higher blocking temperature (200 K) compared to previously reported similar nanoparticles (160 K), indicating enhanced magnetic stability at elevated temperatures. Finally, we demonstrate the practical application of these hybrid magnetic materials as catalysts for carbon monoxide oxidation, showcasing their potential in environmental pollution control and highlighting their versatility as catalyst supports.

KEYWORDS: amyloid fibrils, chitin nanofibrils, magnetic aerogels, hybridization, self-assembly, exfoliation

1. INTRODUCTION

Anthropogenic climate change has disrupted the environment and our communities at an unexpected rate, calling for immediate mitigation actions. Today, it is evident that the current "take—make—dispose" paradigm is no longer viable, and sustainable approaches toward resource safeguarding and cleaner production must be developed. One pivotal strategy within this context involves adopting a circular economy and transitioning from petroleum-based resources to green, sustainable alternatives for materials development.

Every year, 1.3 billion tons of food, equivalent to 30% of the total food produced for human consumption, is wasted.⁶ This waste contributes significantly to climate change, accounting for 8–10% of the global greenhouse gas (GHG) emissions.⁶ Furthermore, plastics-based materials, primarily derived from fossil fuels (>95%),⁷ contribute to an additional 4.5% of GHG emissions.⁸ Eventually, these nonbiodegradable materials become persistent pollutants, adversely affecting both the environment and human health.^{8–11}

In the quest for solutions to this crisis, biopolymers emerge as a promising alternative, particularly when derived from food waste, aligning with the principles of a circular economy. ^{4,6} Biopolymers such as proteins and polysaccharides, abundant in agri-food biomass and sidestreams, offer a compelling opportunity to engineer sustainable advanced materials for addressing global challenges. ^{6,12–15}

Proteins constitute a substantial fraction of the food industries' waste. Hence, valorizing them into a new line of applications represents an ideal strategy. Whey, for instance, is a primary byproduct of the dairy industry. In Europe, where approximately 150 million tons of milk are produced every

Received: January 20, 2024
Revised: February 3, 2024
Accepted: February 6, 2024
Published: February 12, 2024





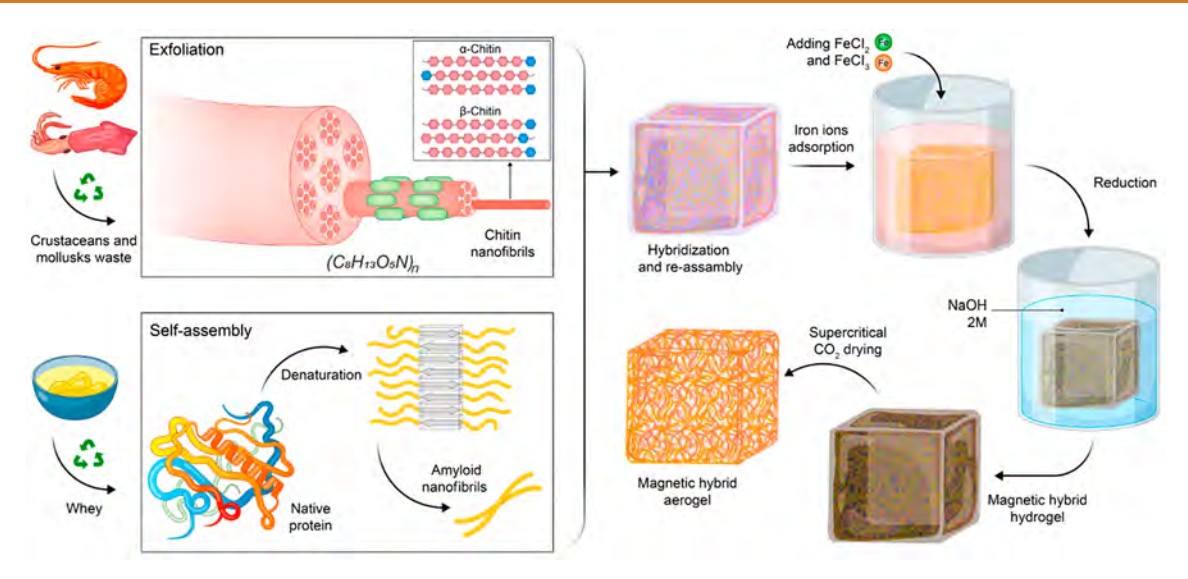


Figure 1. Preparation schematic of hybrid magnetic aerogels made of AF and Ch.

year, 16 half of the milk is utilized in cheese production, yielding a significant volume of liquid whey. Under specific conditions, one can denature the protein in whey, allowing it to self-assemble into amyloid fibrils (AF), 14 an emerging class of fibrillar materials with promising properties that can be harnessed to produce functional materials with exceptional characteristics. AF are composed of repeating core units of peptides and formed by β -sheets packed into β -cross sections perpendicular to the fibril's axis. 14 , 17

On the other hand, chitin, a polymer composed of Nacetylglucosamine (β -1,4-linked 2-acetamido-D-glucose), is the most abundant aminopolysaccharide found in nature, primarily in crustaceans, mollusks, insects, and fungi. 18,19 There are three chitin allomorphs (α -chitin, β -chitin, γ -chitin) with different structural and mechanical properties. ^{19,20} While α -chitin is primarily found in shells and stiff materials, β -chitin and γ -chitin are mostly found in soft and flexible structures. 19 These structural and mechanical variations are attributed to the different arrangements of polysaccharide chains; α -chitin chains align antiparallel to the reducing end, β -chitin chains are parallel, and γ -chitin chains feature a combination of parallel and antiparallel arrangements. 19,21 Chitin accounts for approximately 15–40%²² of the 6–8 million tons of annually produced waste shells from crustaceans such as lobsters, shrimp, and crabs. 19,23 Most of this waste is disposed of into the sea, leading to marine environmental pollution and consequent deterioration in affected ecosystems. 24 However, this seafood waste can be valorized to recover chitin via various mechanical and chemical methods. 19 Exfoliating nanochitin building blocks and reassembling them via bottom-up approaches are viable methods for developing functional materials.²⁵ Depending on the exfoliation method used, one can produce chitin nanofibers, chitin nanofibrils (Ch), and chitin nanocrystals.¹⁹ The main methods involve applying strong mechanical forces or acid hydrolyzation. 19,26 Nanochitins, with their high aspect ratios and large surface areas, provide an excellent opportunity for designing materials through their reassembly for various applications, notably in biomedical and catalysis fields.

Aerogels are an emerging category of superlight weight solid and porous materials that can be obtained by eliminating the solvent from a gel.²⁹ Over the past two decades, the composition of aerogels has mainly comprised inorganic or synthetic

polymers such as silica, metal oxides, or polystyrenes. This has, however, diminished their sustainability and impeded their utilization across various environmental, food, and biomedical applications.²⁹ Recently, the exploration of biobased aerogels derived from biopolymers like polysaccharides and proteins has demonstrated promising characteristics and applications.³⁰ Examples include aerogels derived from cellulose, 31,32 chitin, ^{32,33} bagasse, ³⁴ and proteins. ³⁵ These biobased aerogels can further serve as templates for developing magnetic aerogels. 36,37 In this context, strategically developing aerogels through the hybridization of protein amyloid fibrils and chitin building blocks presents a viable approach to enhancing the properties and functionality of the final materials. This method capitalizes and synergizes the distinct capabilities of each nanobuilding block, fostering the design of 3D materials that merge their distinctive functionalities and properties.

In an earlier study focusing on the hybridization of chitin and proteins, the group of Rolandi incorporated chitin nanofibers into a silk protein fibroin matrix to obtain a biocomposite film that emulates the organic phase of insect cuticles and crustacean exoskeletons.³⁸ The composite exhibited enhanced mechanical properties compared to individual components, thanks to the strong hydrogen bonding between chitin nanofibers and the surrounding silk matrix.³⁸ However, the potential for chitin hybridization with other types of protein nanobuilding blocks remains largely unexplored. While silk serves as a structural protein, exploring the hybridization with self-assembled amyloids through electrostatic complexation could be employed to produce 3D hydrogels and aerogels. Amyloids contribute not only to the formation and reinforcement of the structural network of materials but also, with their inherent high functionality, endow the resulting materials with elevated functionalities. For instance, they can establish biomineralization sites, thereby enabling additional hybridization and introducing heightened complexity and functionality. Additionally, the quest for a more cost-effective protein source as an alternative to silk for hybridization is highly important.

In this study, we develop advanced materials by hybridizing and reassembling Ch and AF. To this end, two types of hybrid materials, i.e., hydrogels and aerogels, are meticulously designed and characterized. To elucidate their functionality, we demonstrate the possibility of manufacturing sustainable

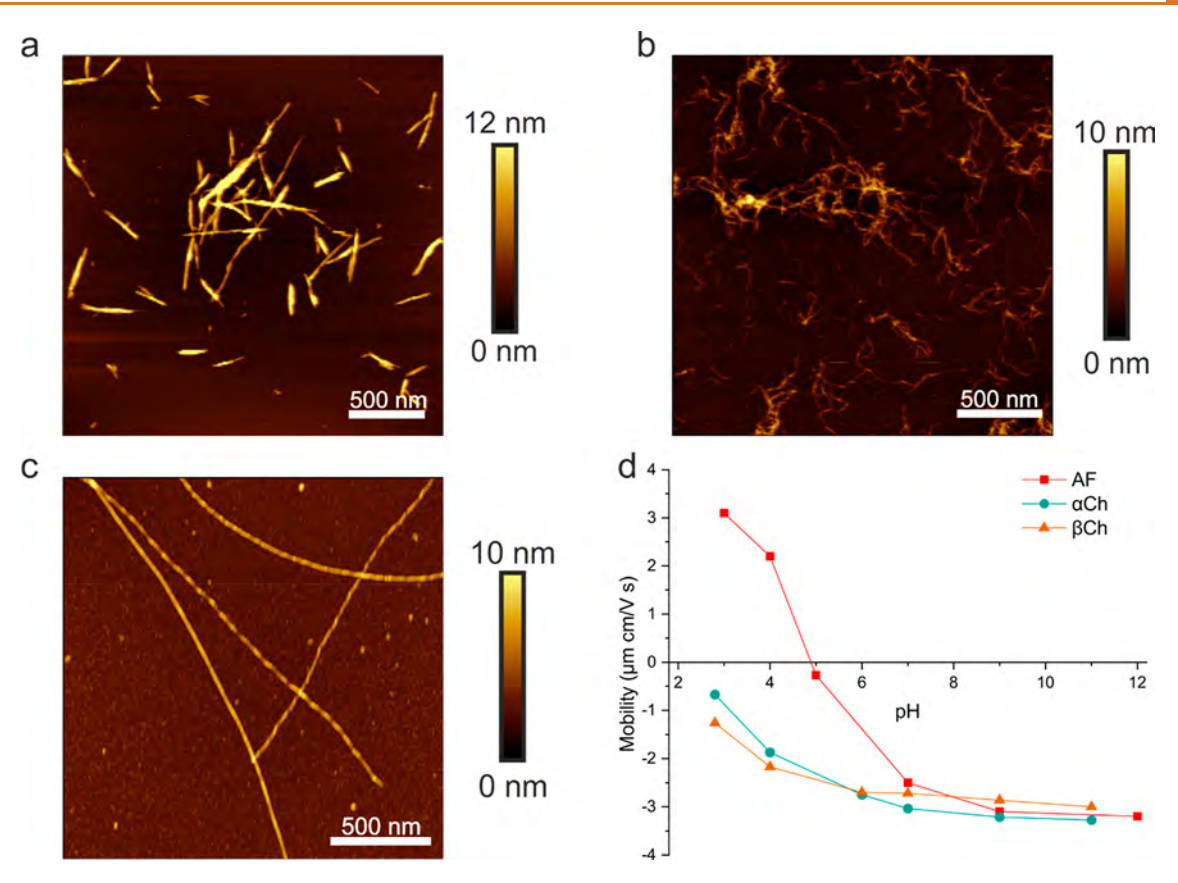


Figure 2. Characterization of exfoliated Ch and self-assembled AF. Representative AFM images of (a) α Ch, (b) β Ch, and (c) AF. (d) Electromobility measurements of AF, α Ch, and β Ch.

magnetic hybrid materials by hybridizing these two valorized biopolymeric nanobuilding blocks and the additional biomineralization of iron nanoparticles. Compared to conventional magnetic hydrogels and aerogels based on silica, polymers, or carbon frameworks,³⁹ the developed hybrid materials exhibit superior sustainability, precisely because they are based on available biomass sidestreams.⁴⁰ Additionally excellent magnetic properties can be endowed to these hybrid materials, and we further demonstrate their use as catalysts for important practical applications such as the oxidation of carbon monoxide.

2. RESULTS AND DISCUSSION

2.1. Biopolymeric Nanobuilding Blocks. The initial step in fabricating hybrid materials involves obtaining biopolymeric nanobuilding blocks, i.e., Ch and AF (Figure 1). To do so, we exfoliated α -chitin nanofibrils (α Ch) and β -chitin nanofibrils (βCh) , sourced from two distinct chitin powders derived from shrimp shells and squid flakes, respectively. Following the purification of chitin powders, the samples were subjected to swelling in a pseudosolvent (dimethyl sulfoxide/potassium hydroxide), followed by exfoliation utilizing mechanical force (ultrasonication). Subsequently, the exfoliated α Ch and β Ch were washed and redispersed in a basic aqueous solution. 41 AFs, on the other hand, were prepared using a different method involving the denaturation and self-assembly of whey protein under acidic conditions at elevated temperatures. 42 For more details on the material synthesis refer to the Materials and Methods (section 4).

Figure 2 presents the characterization of biopolymeric building blocks. α Ch exhibits a rod-like morphology with an aspect ratio of about 33, indicating a closer resemblance to

nanocrystals⁴³ (Figure 2a). In contrast, β Ch, shown in Figure 2b, has a networked structure with flexible fibrils with a significantly higher aspect ratio. AF exhibit the characteristic pattern consisting of long, twisted, and semiflexible fibrillar structures, with contour length extending over several micrometers⁴⁴ (Figure 2c). Figure 2d illustrates the electrophoretic mobilities of AF, α Ch, and β Ch under varying pH conditions. The electrophoretic mobility of AF reaches a point of neutrality (the isoelectric point) at approximately pH 5, indicating a positive charge for AF at pH values below 5 and a shift toward negative charges at pH values above 5.45 For both α Ch and β Ch, the electrophoretic mobility remains consistently negative; however, these negative values appear to increase from pH 2 toward pH 12. This trend suggests the successful esterification of the C₆ molecule of the glucose ring by maleic anhydride (used in the exfoliation step), resulting in the addition of a COO⁻ group, as reported in previous studies. 41,46 This introduced negative charge accounts for the negative electrophoretic values observed for α Ch and β Ch at lower pH levels. 40

2.2. Hybrid Magnetics Hydrogels. First, we evaluated the mixing behavior of AF (2 wt %) with α Ch (1 wt %) and β Ch (0.5 wt %) at different pH values. The phase diagrams depicting the outcomes of mixing AF with α Ch and AF with β Ch are presented in Figures S1 and S2, respectively. These diagrams show three distinct regions: gel, semigel (a weak gel or a solution with a noticeable increase in viscosity), and solution. When blending AF with α Ch, gel formation was observed, particularly at lower initial pH values for AF. This phenomenon highlights the importance of electrostatic interactions, as AF carry a positive charge at these pH values, ⁴⁵ which interact with the negatively charged α Ch. In contrast, at higher pH values, no

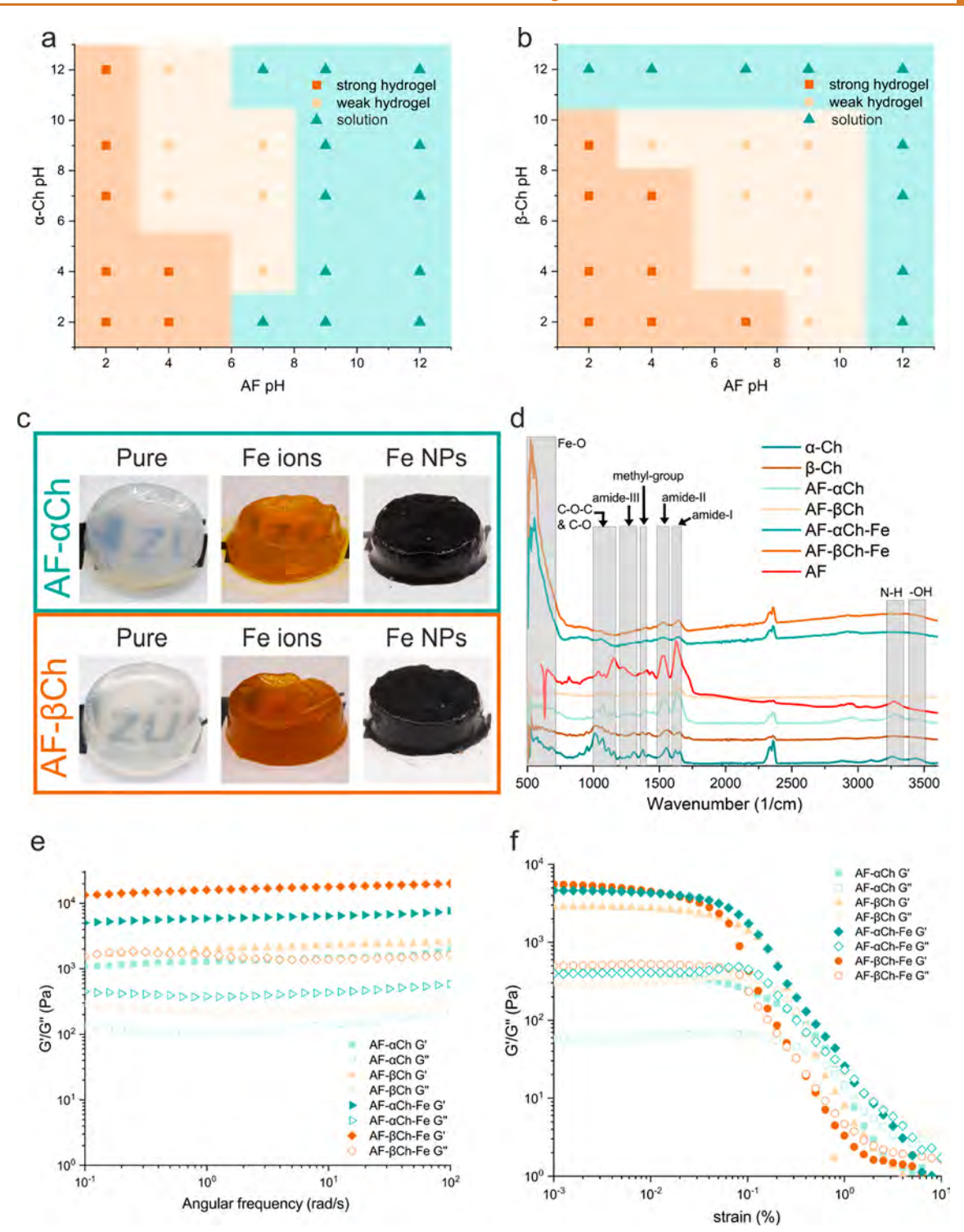


Figure 3. Hybrid chitin—amyloid nanofibrils hydrogels. pH phase diagram for producing hydrogels with salt diffusion for (a) AF- α Ch mixtures and (b) AF- β Ch mixtures. (c) Visual appearance of pure hydrogels (transparent), loaded with Fe ions (brown), and after reduction to Fe NPs (black), where the diameter of the hydrogels was around 2 cm. Characterization of pure and hybrid samples: (d) FTIR, (e) frequency sweep, and (f) strain sweep tests.

gelation occurred as both AF and α Ch carry negative charges. In the case of the AF and β Ch mixture, the semigel and solution regions were predominant. Interestingly, regardless of the initial pH of β Ch, no gel formation was observed when starting with AF at a pH of 2. The observation that the most robust gels were produced when AF was initiated at a pH of 4 (close to the isoelectric point of AF) indicates weak interactions between AF

and β Ch and highlights the neutralization of AF charges at their isoelectric point as the primary gelation mechanism. As the high viscosity of β Ch prevented us from working with a concentration of >0.5 wt %, the lower concentration of β Ch compared to α Ch solutions in the system could also contribute to this mixing behavior (see the viscosity values in Figure S3).

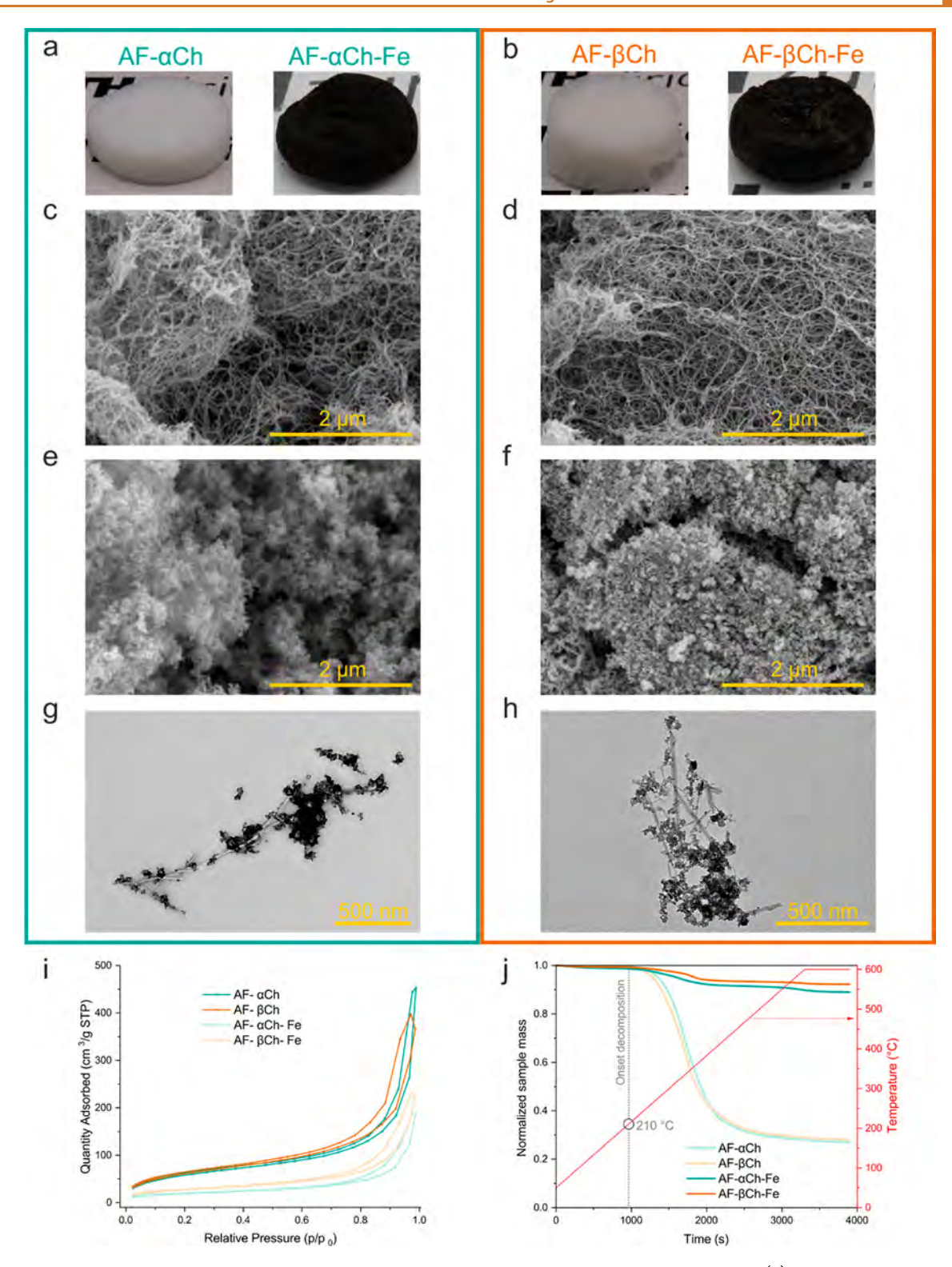


Figure 4. Hybrid chitin—amyloid nanofibrils aerogels. The visual appearance of pure and magnetic aerogels: (a) AF- α Ch mixtures and (b) AF- β Ch mixtures. SEM images of aerogels: (c) pure AF- α Ch, (d) pure AF- β Ch, (e) magnetic AF- α Ch-Fe, and (f) magnetic AF- β Ch-Fe. TEM images of g) magnetic AF- α Ch-Fe and (h) magnetic AF- β Ch-Fe. (i) N₂ sorption isotherms and (j) TGA in N₂ atmosphere for hybrid chitin—amyloid nanofibrils aerogels.

To enhance the robustness of the hydrogels, we further introduced salt diffusion into the mixtures. The salt ions screen the surface charges and thereby promote the aggregation of AF, α Ch, and β Ch. This, in turn, promotes the physical cross-linking of these nanobuilding block's networks and allows us to produce

stable hydrogels.⁴⁷ Following the mixing of the nanobuilding block mixtures at various pH values, we molded and encased them within a dialysis membrane. Subsequently, the encapsulated mixtures were exposed to a 0.35 M NaCl solution. Figure 3a and Figure 3b show the concentration phase diagram of AF-

 α Ch and AF- β Ch hybrid hydrogels produced by salt diffusion, respectively (the related photographs are presented in Figures S4 and S5). As observed, stable hydrogels could be successfully formed at lower initial pH values of AF. However, as the initial pH of AF increased, the stability of the hydrogels was reduced, and eventually, no hydrogels were formed. In the case of the hybrid hydrogels derived from the combination of AF and α Ch (Figure 3a), no robust hydrogels were formed for initial pH values of AF exceeding 6. Likewise, for the hybrid hydrogels formed with AF and β Ch (Figure 3b), no strong hydrogels were obtained when the initial pH of AF exceeded 8. Therefore, we selected AF with an initial pH of 2, as well as α Ch and β Ch with an initial pH of 9, to proceed with the fabrication of the magnetic hydrogels.

To fabricate the magnetic hydrogels, the NaCl solution was replaced with an iron salt solution, here, a mixture of FeCl₂ and FeCl₃ (0.4 M/0.8 M). Following the diffusion of iron ions, we successfully obtained robust, brown, transparent hydrogels (Figure 3c). We further reduced the iron ions by immersing the hydrogels in basic aqueous solutions, resulting in the production of hybrid hydrogels loaded with black Fe₃O₄ nanoparticles, ⁴⁸ for both AF- α Ch (AF- α Ch-Fe) and AF- β Ch (AF- β Ch-Fe), as shown in Figure 3c. Fe₃O₄ particles are ferrimagnetic, with a high saturation magnetization and a low coercivity. ⁴⁹ Their biocompatibility allows for an easy incorporation into the hydrogel while imparting their magnetic properties. ⁵⁰ This was confirmed by moving the Fe₃O₄-loaded hydrogels with a magnet, as demonstrated in Video S1.

Figure 3d presents the Fourier transform infrared (FTIR) spectra for each nanobuilding block and the resulting hybrid materials. The peaks at 1633 cm⁻¹ and 1523 cm⁻¹ and the broadband spanning 3200 and 3600 \mbox{cm}^{-1} are indicative of the amide I, 12,51,52 amide II, 12,51,52 and -OH stretching bands, 52,53 which are consistently present in all three building blocks: α Ch, β Ch, and AF. A further split peak in the amide-I peak can be observed for α Ch, which is its characteristic and differs from the amide-I peak for β Ch.³⁸ The peak at 1229 cm⁻¹ is a characteristic marker of the amide III band in AF, 12,52 while for α Ch and β Ch this band appears at 1310 cm^{-1,38} Peaks at 1155 cm⁻¹,1113 cm⁻¹, 1067 cm⁻¹, and 1032 cm⁻¹ correspond to the stretching of C-O-C and CO. Another peak at 1377 cm⁻¹ corresponds to the methyl groups vibrational absorption.⁵⁴ Furthermore, the peak at 3250 cm⁻¹ corresponds to the NH stretching bands of Ch.^{51,55} Finally, the peak at 570 cm⁻¹, corresponding to the Fe-O bonds, ⁵⁶ along with the obtained Xray diffraction (XRD) pattern (Figure S6), confirms the presence of Fe₃O₄ in the magnetic AF and α Ch or β Ch hybrid aerogels.

To assess the mechanical stability of the magnetic and nonmagnetic hydrogels, we performed the frequency and strain sweeps (Figure 3e,f). The storage modulus (G') and the loss modulus (G'') appear to be frequency-independent,⁵⁷ where G' was 1 order of magnitude larger than G'' for all hydrogels, showing the solid-like nature of the materials (Figure 3e). The magnetic hydrogels showed a higher G' and G'' for both types of hybrid material, where the variation of AF- β Ch was the highest for both the magnetic and the nonmagnetic version (Figure 3e). This could be due to the higher mechanical flexibility of β Ch compared to α Ch (Figure 2b,c), which impacts the hybrid hydrogels' network structure and, thus, mechanical stability. Figure 3f shows that both Fe₃O₄-hydrogel variations were more stable and failed at a higher strain [%] than the nonmagnetic hydrogels. Interestingly, both AF- α Ch hydrogels withstood

higher strain deformation before failing to mitigate the stress (Figure 3f). ⁵⁹

2.3. Hybrid Magnetics Aerogels. We transformed the stable hybrid hydrogels into aerogels using supercritical CO2 drying. Figure 4a and Figure 4b show the hybrid aerogels for AFlphaCh and its magnetic counterpart AF-lphaCh-Fe, as well as for AF- β Ch and its magnetic counterpart AF- β Ch-Fe, respectively. The resulting aerogels were uniform and mechanically stable. Scanning electron microscopy (SEM) images of the hybrid aerogels are presented in Figure 4c-f. From Figure 4c,d, it can be concluded that both AF- α Ch and AF- β Ch hybrid aerogels exhibited internal fibrillar networks. 45,60 Following the biomineralization process, these networks were covered by Fe₃O₄ nanoparticles, 61 as shown in Figure 4e,f. From a more detailed examination of fragments of these structures using transmission electron microscopy (TEM), it is clear in Figure 4g,h that the fibrillar structures in both AF- α Ch-Fe and AF- β Ch-Fe were coated with Fe₃O₄ nanoparticles. The nanoparticles tended to form clusters and distribute along the fibrillar structures. At the aerogel levels, the iron oxide nanoparticles are predominantly distributed within the intercalations, covering the spaces within the aerogels (Figure S7). The size of individual Fe₃O₄ nanoparticles was estimated to be between 5 and 25 nm; from XRD measurements of AF- α Ch-Fe the average crystallite size of Fe₃O₄ was around 8 nm (calculated using the Scherrer equation).

To elucidate the porosity and surface characteristics of the hybrid aerogels, we conducted N_2 adsorption—desorption analysis (Figure 4i), from which we derived the Brunauer—Emmett—Teller (BET) surface areas, pore volumes, and pore sizes based on the Barrett—Joyner—Halenda (BJH) method (Table 1). The N_2 sorption isotherms of hybrid aerogels

Table 1. BET Surface Areas, BJH Pore Volumes, and Average Pore Sizes of Hybrid Aerogels

	$S_{ m BET}$	$V_{ m p}$	pore size
	(m^2/g)	$\left(\text{cm}^3/\text{g}\right)$	(nm)
AF- $lpha$ Ch	212	0.646	4.4
AF- β Ch	223	0.571	24.5
AF- α Ch-Fe	67	0.288	11.3
AF-βCh-Fe	97	0.350	11.1

exhibited a type IV adsorption isotherm in accordance with the IUPAC isotherm categorization, implying the presence of a mesoporous network.⁶² Furthermore, the observed hysteresis shape indicates slit-shaped pores akin to a type H3 hysteresis loop. 62 The higher adsorption and desorption values for AF-Ch compared to AF-Ch-Fe hybrid aerogels reveal the larger surface area of the nonmagnetic aerogels compared to their magnetic counterparts. Specifically, the BET surface areas of AF- α Ch and AF- β Ch turned out to be 212 and 223 m²/g, respectively, i.e., notably larger than the respective values for AF- α Ch-Fe and AF- β Ch-Fe, which were 67 and 97 m²/g. This reduction in surface area and pore volumes can be attributed primarily to the partial occlusion of the aerogel pores by the Fe₃O₄ nanoparticles.⁶³ Additionally, the slightly higher surface area of AF- β Ch compared to AF- α Ch is attributable to its crystal lattice structure, which imparts the former a more open and accessible structure. 64 Intriguingly, although the pore sizes of AF- α Ch and AF- β Ch hybrid aerogels differed, both magnetic hybrid aerogels had pore sizes of approximately 11 nm (Table 1).

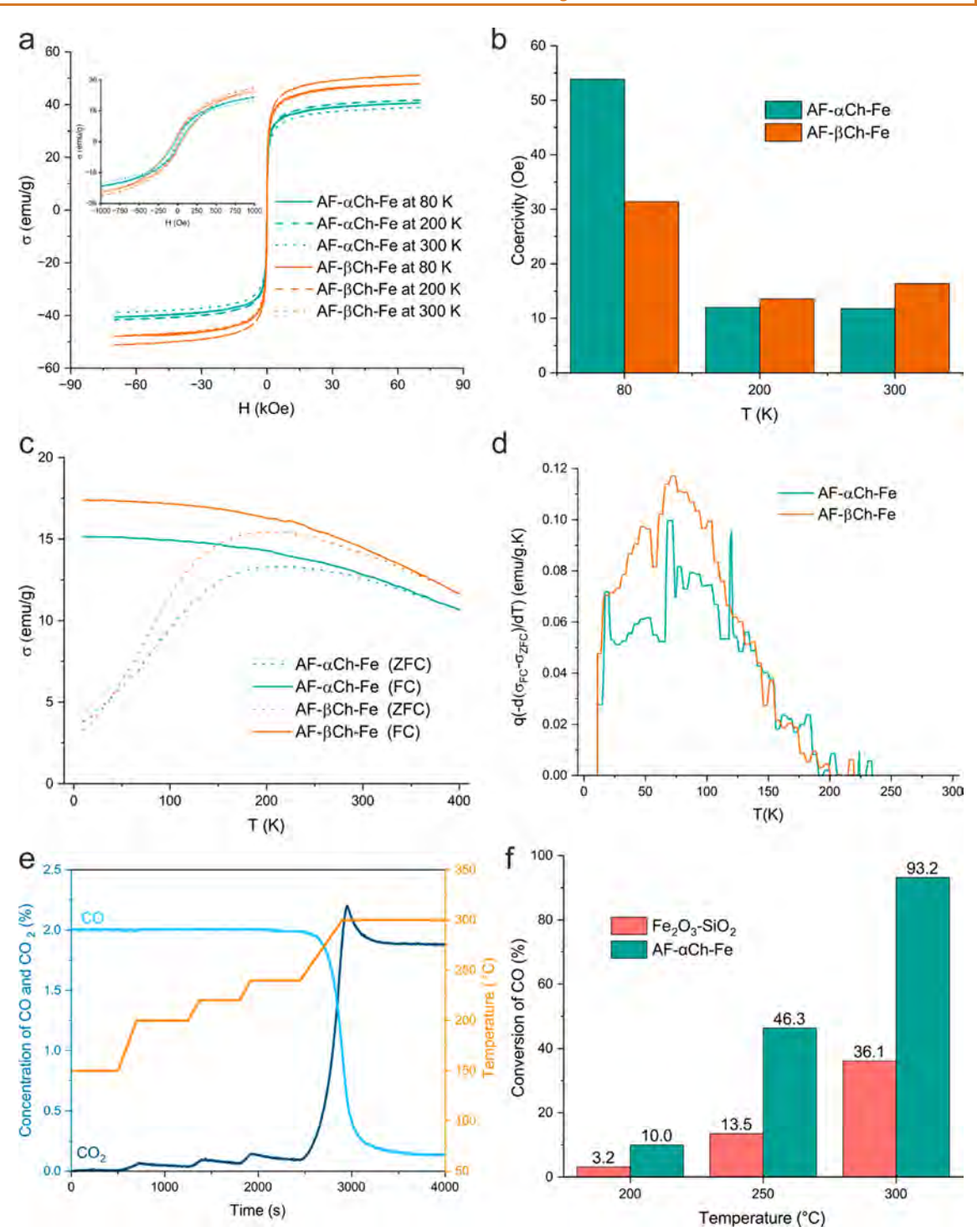


Figure 5. Magnetic and catalytic properties of the AF- α Ch-Fe and AF- β Ch-Fe aerogels. (a) Magnetic hysteresis curves taken at 80, 200, and 300 K for AF- α Ch-Fe and AF- β Ch-Fe (inset: zoomed-in magnetic hysteresis curves). (b) Temperature-dependent coercivity for both AF- α Ch-Fe and AF- β Ch-Fe. (c) FC and ZFC magnetization curves measured at an external field of 100 Oe for AF- α Ch-Fe and AF- β Ch-Fe. (d) Field-derivative of the difference between the FC and ZFC magnetization curves for AF- α Ch-Fe and AF- β Ch-Fe. (e) Concentrations of CO and CO₂ over time and as a function of temperature using the AF- α Ch-Fe aerogel as a catalyst. (f) Catalytic performance comparison of the AF- α Ch-Fe aerogel versus Fe₂O₃-SiO₂.

Figures 4j and S8 show the results of the thermogravimetric analysis (TGA) of the magnetic and nonmagnetic hybrid aerogels when heating them in N_2 or air up to 600 °C. The AFCh hybrid aerogels started to decompose at temperatures of >210 °C, regardless of the environment (N_2 or air). The onset temperature of the decomposition was not influenced by the presence of Fe_3O_4 nanoparticles. In N_2 under pyrolysis

conditions, the total weight loss of both AF-Ch hybrid aerogels was \sim 72%, whereas in the air (under combustion conditions), the total weight loss was \sim 90% when reaching 600 °C. During the measurements with the AF-Ch-Fe hybrid aerogels, Fe₃O₄ was gradually oxidized to Fe₂O₃ above \sim 105 °C. From these TGA measurements, the weight ratio of Fe₃O₄ to the AF-Ch

hybrid aerogel skeleton can be estimated, giving 86:14 wt % for Fe₃O₄:AF- α Ch and 90:10 wt % for Fe₃O₄:AF- β Ch.

2.4. Magnetic Properties. The magnetic hysteresis curves of AF- α Ch-Fe and AF- β Ch-Fe indicate that, at all temperatures, both samples exhibit ferromagnetic behavior with a very small coercivity of <50 Oe and a high specific magnetization of >40 emu/g (Figure 5a,b). The small coercivity and the strong magnetic response suggest that these nanoparticles could potentially be useful for superparamagnetic applications.⁴⁹ Several further insights can be obtained from our results. First, the temperature-dependent behavior of AF-αCh-Fe and AF- β Ch-Fe (Figure 5c) was qualitatively similar to each other. The behavior of both samples was qualitatively also similar to the control sample of the pure Fe₃O₄ nanoparticles used in our study (Figure S9), albeit with a lower specific magnetization due to the additional mass of nonmagnetic chitin. Hence, we conclude that the AF and Ch, made of a nonmagnetic material, did not have any magnetic interactions with the Fe₃O₄ nanoparticles. Second, the temperature-dependent behavior of AF- α Ch-Fe and AF- β Ch-Fe demonstrated a clear magnetic transition where the zero-field-cooled (ZFC) and field-cooled (FC) curves began to diverge (Figure 5c). This transition can be characterized by a blocking temperature $(T_{\rm B})$ of approximately 200 K, defined as the temperature at which the ZFC magnetization shows a maximum. The observed $T_{\rm B}$ value in our case is slightly higher than the 160 K value previously reported for a similar Fe₃O₄ nanoparticle system⁶⁵ and an order of magnitude higher than the theoretically predicted $T_{\rm B}$ of noninteracting particles.⁶⁶ The higher transition temperature can be explained by magnetic interactions among the nanoparticles, which increase the effective anisotropy energy barriers for magnetization reversal. 66

To gain more insight into the magnetic interactions, in Figure 5d we plot the derivative of the difference between the ZFC and FC curves. Such derivative is proportional to the distribution of anisotropy energies in the system. Unlike the Gaussian distribution expected for a random distribution of nanoparticle sizes, the distribution of anisotropy energies in our case was clearly skewed toward higher temperatures, interpreted as a signature of magnetic interactions. The AF- α Ch-Fe and AF- β Ch-Fe had similar distributions of anisotropy energies, indicating that the differences in the chitin structure did not affect the magnetic interactions between the nanoparticles.

2.5. Catalytic Applications. We further used the magnetic AF- α Ch-Fe aerogel as a catalyst for the oxidation of CO to CO₂. We note that iron-based catalysts are not among the best materials for this reaction, ⁶⁸ but iron oxide has been used as an inexpensive, active support providing reactive oxygen ⁶⁹ for precious metal catalysts such as Au or Pd. ^{70–73} However, there have been several studies using nanosized iron oxide without precious metals (in particular for the CO oxidation at higher temperatures, ~300 °C), indicating that high surface areas and small iron oxide crystal sizes are required for high CO conversions. ^{74,75}

Figure 5e shows the conversion of CO over time and as a function of the temperature for the AF- α Ch-Fe aerogel. The conversion increased markedly above 250 °C (catalyst light off temperature), similar to observations made in previous studies using commercial iron oxide nanoparticles. At 300 °C, the CO conversion was 93%. A comparison with a reference catalyst, α -Fe₂O₃ on Aerosil 300, is given in Figure 5f, showing that the AF- α Ch-Fe aerogel performed significantly better, which may have been partially due to the smaller crystallite size of the iron oxide in the AF- α Ch-Fe aerogel (around 8 nm for AF- α Ch-Fe versus

40 nm for α -Fe₂O₃ on Aerosil 300, calculated using the Scherrer equation and XRD measurements in Figure S6). Importantly, the original black Fe₃O₄ nanoparticles transformed into redbrown γ-Fe₂O₃ during the catalytic oxidation of CO due to an excess of oxygen (Figure S6). γ-Fe₂O₃ has frequently been reported to possess better redox properties than α -Fe₂O₃, which would result in a better catalyst performance. 77,78 For small Fe₃O₄ particles (<300 nm) as in the AF- α Ch-Fe aerogel, γ -Fe₂O₃ is the thermodynamically favored oxidation product, and a further transformation is not expected below 400-500 °C.80-82 Lastly, the TGA measurements in Figure S8 have shown that AF- α Ch decomposes above ~210 °C. The overshoot in CO₂ concentration at ~3000 s in Figure 5e suggests that indeed some of the carbon in the material was oxidized to CO₂. The strategy employed in this study could potentially be extended to synthesize other catalytic materials, such as Au/Fe₂O₃ nanoparticles, ⁸³ achieving lower CO oxidation temperatures and preserving the integrity of the biopolymeric scaffold. This is expected to facilitate the development of multifunctional catalytic systems with enhanced performance and structural stability.

3. CONCLUSIONS

In summary, we demonstrated the development of advanced materials with enhanced properties and functionalities through the hybridization and reassembly of biopolymeric nanobuilding blocks valorized from dairy and seafood waste. We engineered various hybrid hydrogels and aerogels by hybridizing AF and Ch, meticulously evaluating their formation by assessing the mixing behavior, salt diffusion, and biomineralization. The resulting hybrid magnetic materials, achieved through the biomineralization of iron nanoparticles, exhibit exceptional magnetic properties characterized by distinct ferromagnetic traits and minimal coercivity, affirming their suitability for superparamagnetic applications. Moreover, we successfully demonstrated the practical application of these hybrid materials as catalysts for converting carbon monoxide, thus addressing possible environmental pollution applications. This work not only underscores the extensive potential of sustainable biopolymeric nanobuilding blocks for designing innovative materials, but also highlights their pivotal role in waste management, contributing significantly to the global endeavor for a circular and sustainable economy that aligns advanced materials with environmental responsibility.

4. MATERIALS AND METHODS

4.1. Materials. Chitin powder from shrimp shells of practical grade was purchased from Sigma-Aldrich. Chitin from squid flakes was purchased from Glentham Life Science. Whey protein isolate was provided from Fonterra and directly used for the preparation of amyloid nanofibrils. Hydrochloric acid (37%), sodium hydroxide (NaOH), sodium hypochlorite (NaOCl, 14%), dimethyl sulfoxide (DMSO), ethanol (99.9%), potassium hydroxide (KOH), and maleic anhydride (MAH) were purchased from Sigma-Aldrich. Sodium chloride (NaCl), iron(III) chloride hexahydrate (FeCl₃·6H₂O), iron(II) chloride tetrahydrate (FeCl₂·4H₂O), and iron(III) oxide (FeCl₃) were supplied by Sigma-Aldrich and used for the production of hybrid hydrogels. Aerosil 300 was purchased from Evonik Industries.

4.2. Methods. *4.2.1. AF Production.* First, a 2 wt % whey solution was prepared by dissolving 10 g of whey protein powder into 490 mL of Milli-Q water. The pH of the solution was then adjusted to 2 by using a 1 M HCl solution. Afterward, to transform the native protein to AF, 84 the solution was incubated at 90 °C for 5 h. Then, the AF solution was quenched and kept in a cold room for further use.

4.2.2. Chitin Powder Purification. Both the chitin powders from shrimp shells and the squid flakes were purified separately. The squid flakes were first milled into a powder-like material using a rotator mill (Retsch, Mu2, ultracentrifuge, B13, TE, Germany) using a pore size of 0.25 mm. For the first step of the purification process, the chitin powder (50 mg/mL) was dissolved in a 0.25 M HCl solution and stirred for 2 h. Afterward, the demineralized chitin samples were washed with Milli-Q water and centrifuged (MPW Med. Instruments, MPW-380R, Poland) at 14 000 rpm for 10 min. Subsequently, the wet chitin (50 mg/mL) was redispersed in a 2 M NaOH solution at 50 °C for 2 h. The deproteinized chitin was washed with Milli-Q water and centrifuged (14 000 rpm, 10 min). Finally, the wet chitin mass (25 mg/mL) was bleached by resuspending it in a 2% NaOCl solution at pH 5 for 30 min. After bleaching, the chitin mass was washed with Milli-Q water and centrifuged. 19,85 The purified chitin was left to dry at room temperature for 24 h.

4.2.3. Chitin Exfoliation. The chitin powder was added to DMSO/KOH (α-chitin 20 mg/mL, β-chitin 4 mg/mL), which acts as a pseudosolvent. To produce this pseudosolvent, DMSO was saturated with KOH (1 mg/mL). Hen the α-chitin and β-chitin were swelled for 24 and 3 h, respectively. After swelling, the samples were further ultrasonicated (Hielscher Ultraschall-Technologie, UP200H, Germany) for 30 min with an amplitude of 90% and a cycle duration of $0.5 \, {\rm s}^{-1}$. Subsequently, MAH was added, and the samples were stirred for 1 min at room temperature. Then, the samples were washed and centrifuged once with DMSO (14 000 rpm, 5 min) and once with ethanol (14 000 rpm, 5 min). Next, the samples of αCh (10 mg/mL) and βCh (5 mg/mL) were redispersed into a NaOH solution at pH 11 and stirred for 1 h. 19,41 For βCh, redispersion into the NaOH solution was the last step. In contrast, αCh was centrifuged at 4000 rpm for 10 min, and the so-produced supernatant was recovered, while the residue was discarded. 41,86

4.2.4. Evaluation of Mixing Behavior of AF and Chs. To screen for gelling conditions of the AF-Ch building blocks, the mixing outcome of the AF and Chs solutions at various pH values was studied. The α Ch (1 wt %), β Ch (0.5 wt %), and AF (2 wt %) solutions were prepared at various pHs (2, 4, 7, 9, 12). All combination AF samples with α Ch or β Ch samples were tested by mixing the two components in equal proportions within 4 mL glass vials. The vials were then left for 24 h at room temperature.

4.2.5. Fabrication of Hybrid Hydrogels by Salt Diffusion. Following the individual mixing of AF with both α Ch and β Ch at five distinct pH values (2, 4, 7, 9, 12), the resultant samples (1 mL) were introduced into a 10 mL syringe. A dialysis membrane (MWCO 6–8 kDa, Spectra/Por, Spectrum Laboratories Inc.) was securely attached to the syringe's opening. The loaded syringe was then submerged in a 350 mM NaCl solution and affixed to the container's cap. ⁴⁷ They were then left to react for 48 h. Finally, the hybrid aerogels were retrieved by carefully extruding them from the syringe after the dialysis membrane.

4.2.6. Fabrication of Magnetic Hybrid Hydrogels. The fabrication of magnetic hybrid hydrogels followed the methods outlined previously in section 4.2.5, with the modification of substituting the NaCl solution with a solution composed of FeCl $_3$ ·6H $_2$ O/FeCl $_2$ ·4H $_2$ O (0.4 M/0.8 M). Subsequently, the hydrogels were directly transferred into a Petri dish containing 2 M NaOH, leading to the formation of hydrogels loaded with Fe $_3$ O $_4$ nanoparticles. ⁵⁰

4.2.7. Fabrication of Hybrid Aerogels. The hydrogels were converted to aerogels by supercritical CO_2 drying (Autosamdri-931, Tousimis Research Corporation). First, a solvent exchange was carried out stepwise, starting from a 10% ethanol and 90% Milli-Q water mixture. For each step, the hydrogels were left in the respective ethanol and Milli-Q water mixture for 4 h. Finally, in the last step, the hydrogels were immersed in pure ethanol. After the solvent exchange, the magnetic and the nonmagnetic hydrogels were subjected to the supercritical CO_2 drying process. 87,88

4.2.8. Characterization. For AFM examination, the AF and Ch solutions were diluted into pH 2 Milli-Q water. 20 μ L solutions with a concentration of 0.01 wt % were deposited onto freshly cleaved mica surfaces for AF, and onto APTES-coated mica for Ch. After an incubation period of 1 min, the samples were gently rinsed with Milli-Q

water, air-dried, and subsequently scanned in ambient conditions using tapping mode using a Bruker MultiMode VIII scanning probe microscope. The electrophoretic mobility of AF and Ch was measured by using a Malvern Nano-Zetasizer. FTIR spectra spanning the range from 500 to 4000 cm⁻¹ were obtained using a Nicolet iS50 FTIR spectrometer (Thermo Scientific) equipped with an ATR module. We used a rheometer AR 2000 (TA Instruments) to perform frequency sweep and strain sweep tests. A plate-plate geometry with a diameter of 20 mm was used in all of the measurements. All of the experiments were performed at room temperature. To avoid evaporation during the measurements, a solvent trap was used to cover the sample. We performed the frequency sweep tests at a fixed strain of 0.001%, which is within the linear viscoelastic region (see Figure 3f). For the AF and α Ch or β Ch hybrid hydrogels, gap sizes of 3.6 and 4 mm were used. For the AF and α Ch or β Ch hybrid Fe₃O₄-loaded hydrogels, gap sizes of 3.8 mm and 4.9 mm were used. The angular frequency for the strain sweep experiments was fixed at 6.238 rad/s. For the AF and α Ch or β Ch hybrid hydrogels, 4.2 and 3 mm gap sizes were used, while for the AF and α Ch or β Ch hybrid Fe₃O₄-loaded hydrogels, gap sizes of 3 and 4 mm were used. To examine the internal structure of aerogels, a Hitachi SU5000 SEM was employed. Prior to the SEM imaging process, small sections of the aerogels were coated with a 5 nm layer of platinum/ palladium using a planetary system (Safematic, CCU-10, Switzerland). For the TEM measurements, samples of aerogel carrying Fenanoparticles were redissolved in Milli-Q water at pH 2 to obtain a suspension of estimated 2 mg/mL. Samples were suspended overnight to ensure a complete rehydration. For sample fixation, 4 μ L of sample solution was loaded onto negatively charged carbon-coated copper grids for 1 min. The staining was achieved at 5 μ L of 2% uranyl acetate for 15 s and repeated twice. The images were taken by bright-field TEM (FEI, Morgagni 268, USA) operated at a voltage of 100 kV. The specific surface area and pore volume were assessed through N2 adsorption analysis conducted at −196 °C using an Anton Paar Nova 800 instrument. The specific surface area of the samples was calculated by using the BET method. The total pore volume was determined based on the quantity of nitrogen adsorbed at $p/p_0 = 0.96$. To calculate the pore size, the BJH method was applied, presuming slit-shaped pores, and this analysis was performed by using a Micrometrics 3Flex instrument. Prior to the BET analysis, the samples were subjected to degassing at 150 °C for 5 h under vacuum, whereas for BJH analysis, degassing was carried out under vacuum conditions at 100 °C using a Micrometrics SmartVacPrep system. Thermal characteristics of the aerogel were assessed by using a TGA instrument (Mettler Toledo TGA/DSC 3+). The measurements were conducted using a programmed temperature sequence, starting at 25 °C with a 5 min hold, followed by heating to 600 °C at a rate of 10 °C/min, and finally, a 10 min hold at 600 °C. These analyses were carried out in 150 μ L alumina crucibles, under either air or nitrogen gas flow. Before commencing the measurements, the aerogel was preconditioned at 100 °C for 30 min to remove any adsorbed moisture. The XRD analysis was performed using a PANalytical Empyrean X-ray diffractometer, which employed Bragg-Brentano HD incident beam optics with Cu Kα radiation (wavelength of 1.5418 Å, 45 kV, and 40 mA), and an X'Celerator Scientific ultrafast line detector. A monochromator was installed to suppress fluorescence originating from the iron-containing samples. The measurements covered the 2θ range of $20-80^{\circ}$ with a step size of 0.0167° , and the total duration of the measurement was 6 h. Magnetization measurements were performed using the Quantum Design MPMS-XL magnetometer with the reciprocating sample option (RSO) mode enabled. The FC measurements were performed by first cooling the sample in an external magnetic field and then by collecting the data upon warming. The ZFC measurements were performed by first cooling down the sample in a zero magnetic field, then by applying the magnetic field, and finally by collecting the data upon warming.

4.2.9. Catalytic Measurements. The catalytic measurements (oxidation of CO, 2CO + $O_2 \rightarrow 2CO_2$) were carried out in a packed bed reactor (quartz tube, inner diameter 8 mm) housed in an electrically heated furnace. The sample was placed in the isothermal zone of the reactor, covering a length of $\sim\!2$ cm. The furnace temperature was controlled through a type K thermocouple located

ACS Nano www.acsnano.org Article

outside the quartz tube. Separate temperature calibration measurements with an additional thermocouple placed in the center of the sample bed showed temperature differences <4 °C between the two thermocouples over the temperature range of 50–300 °C; during the actual catalytic measurements, there was no thermocouple inside the sample bed. The total gas flow rate through the reactor was 50 mL/min, as measured and controlled at ambient temperature and pressure using mass flow controllers (Bronkhorst EL-flow series). The gas composition was either pure $\rm N_2$ when purging the reactor or a mixture of $\rm O_2/CO/N_2$ (12.5/2/85.5%) when assessing the catalytic performance of the material. The off-gas from the packed bed was measured by using infrared sensors for CO and CO₂ (ABB EL3020, Uras 26).

ASSOCIATED CONTENT

Supporting Information

The Supporting Information is available free of charge at https://pubs.acs.org/doi/10.1021/acsnano.4c00883.

pH phase diagram upon mixing AF and α Ch and AF and β Ch; viscosity values for α Ch and β Ch; visual pH phase diagram for producing hybrid AF- α Ch and AF- β Ch hydrogels with salt diffusion; XRD results of AF- α Ch-Fe and Fe₂O₃-SiO₂; TEM image of Fe distribution within the AF-Ch-Fe aerogel; TGA in air atmosphere for hybrid AF-Ch and AF-Ch-Fe aerogels; FC and ZFC magnetization curves for Fe nanoparticles (PDF)

Video S1 showing hydrogel being moved by a magnet (MP4)

AUTHOR INFORMATION

Corresponding Authors

Mohammad Peydayesh — Department of Health Sciences and Technology, ETH Zurich, 8092 Zurich, Switzerland; orcid.org/0000-0002-6265-3811; Email: mohammad.peydayesh@hest.ethz.ch

Raffaele Mezzenga — Department of Health Sciences and Technology, ETH Zurich, 8092 Zurich, Switzerland; Department of Materials, ETH Zurich, 8093 Zurich, Switzerland; orcid.org/0000-0002-5739-2610; Email: raffaele.mezzenga@hest.ethz.ch

Authors

Enrico Boschi — Department of Health Sciences and Technology, ETH Zurich, 8092 Zurich, Switzerland; Laboratory for Cellulose & Wood Materials, Empa-Swiss Federal Laboratories for Materials Science and Technology, 8600 Dübendorf, Switzerland; Department of Plant and Environmental Sciences, University of Copenhagen, 1871 Frederiksberg C, Denmark

Massimo Bagnani — Department of Health Sciences and Technology, ETH Zurich, 8092 Zurich, Switzerland; orcid.org/0000-0002-1326-1600

Daniel Tay – Laboratorium für Festkörperphysik, ETH Zürich, CH-8093 Zürich, Switzerland

Felix Donat — Department of Mechanical and Process Engineering, ETH Zürich, CH-8092 Zürich, Switzerland; o orcid.org/0000-0002-3940-9183

Hamed Almohammadi — Department of Health Sciences and Technology, ETH Zurich, 8092 Zurich, Switzerland

Mingqin Li – Department of Health Sciences and Technology, ETH Zurich, 8092 Zurich, Switzerland

Mattia Usuelli — Department of Health Sciences and Technology, ETH Zurich, 8092 Zurich, Switzerland; orcid.org/0000-0003-1459-7250 Toni Shiroka — Laboratorium für Festkörperphysik, ETH Zürich, CH-8093 Zürich, Switzerland; Laboratory for Muon Spin Spectroscopy, Paul Scherrer Institute, CH-5232 Villigen, Switzerland; orcid.org/0000-0001-8624-2649

Complete contact information is available at: https://pubs.acs.org/10.1021/acsnano.4c00883

Author Contributions

M.P. and R.M. conceptualized the project, supervised the research, and designed studies. M.P. and E.B. performed the experiments from nanobuilding block preparation to hybrid materials fabrication and characterization. M.B. and E.B. carried out the AFM measurement. D.T. and T.S. carried out the magnetometry. F.D. carried out $\rm N_2$ sorption, TGA, and XRD measurements as well as the catalytic experiments. H.A. and E.B. carried out the rheology measurements. M.L. carried out the TEM measurement. M.U. and E.B. carried out the supercritical $\rm CO_2$ drying. All authors contributed to evaluating data and writing the final version.

Notes

The authors declare no competing financial interest.

ACKNOWLEDGMENTS

The authors acknowledge the support of the Scientific Center for Optical and Electron Microscopy (ScopeM) of ETH Zurich.

REFERENCES

- (1) Munaweera, T. I. K.; Jayawardana, N. U.; Rajaratnam, R.; Dissanayake, N. Modern plant biotechnology as a strategy in addressing climate change and attaining food security. *Agriculture & Food Security* **2022**, *11* (1), 26.
- (2) Kogo, B. K.; Kumar, L.; Koech, R. Climate change and variability in Kenya: a review of impacts on agriculture and food security. *Environment, Development and Sustainability* **2021**, 23 (1), 23–43.
- (3) Allais, R.; Roucoules, L.; Reyes, T. Governance maturity grid: a transition method for integrating sustainability into companies? *Journal of Cleaner Production* **2017**, *140*, 213–226.
- (4) Muscat, A.; de Olde, E. M.; Ripoll-Bosch, R.; Van Zanten, H. H. E.; Metze, T. A. P.; Termeer, C. J. A. M.; van Ittersum, M. K.; de Boer, I. J. M. Principles, drivers and opportunities of a circular bioeconomy. *Nature Food* **2021**, *2* (8), 561–566.
- (5) Haas, W.; Krausmann, F.; Wiedenhofer, D.; Heinz, M. How Circular is the Global Economy?: An Assessment of Material Flows, Waste Production, and Recycling in the European Union and the World in 2005. *Journal of Industrial Ecology* **2015**, *19* (5), 765–777.
- (6) Peydayesh, M.; Bagnani, M.; Soon, W. L.; Mezzenga, R. Turning Food Protein Waste into Sustainable Technologies. *Chem. Rev.* **2023**, 123 (5), 2112–2154.
- (7) Chow, J.; Perez-Garcia, P.; Dierkes, R.; Streit, W. R. Microbial enzymes will offer limited solutions to the global plastic pollution crisis. *Microbial Biotechnology* **2023**, *16* (2), 195–217.
- (8) Stegmann, P.; Daioglou, V.; Londo, M.; van Vuuren, D. P.; Junginger, M. Plastic futures and their CO2 emissions. *Nature* **2022**, *612* (7939), 272–276.
- (9) Li, Y.; Tao, L.; Wang, Q.; Wang, F.; Li, G.; Song, M. Potential Health Impact of Microplastics: A Review of Environmental Distribution, Human Exposure, and Toxic Effects. *Environment & Health* **2023**, 1 (4), 249–257.
- (10) Peydayesh, M.; Bagnani, M.; Mezzenga, R. Sustainable Bioplastics from Amyloid Fibril-Biodegradable Polymer Blends. ACS Sustainable Chem. Eng. 2021, 9 (35), 11916–11926.
- (11) Ramesh, P.; Vinodh, S. State of art review on Life Cycle Assessment of polymers. *International Journal of Sustainable Engineering* **2020**, *1*3 (6), 411–422.

- (12) Peydayesh, M.; Vogt, J.; Chen, X.; Zhou, J.; Donat, F.; Bagnani, M.; Müller, C. R.; Mezzenga, R. Amyloid-based carbon aerogels for water purification. *Chemical Engineering Journal* **2022**, 449, 137703.
- (13) Bagnani, M.; Ehrengruber, S.; Soon, W. L.; Peydayesh, M.; Miserez, A.; Mezzenga, R. Rapeseed Cake Valorization into Bioplastics Based on Protein Amyloid Fibrils. *Advanced Materials Technologies* **2023**, *8* (3), 2200932 (accessed Oct 26, 2023).
- (14) Peydayesh, M.; Mezzenga, R. Protein nanofibrils for next generation sustainable water purification. *Nat. Commun.* **2021**, *12* (1), 3248.
- (15) Nakajima, H.; Dijkstra, P.; Loos, K. The Recent Developments in Biobased Polymers toward General and Engineering Applications: Polymers that are Upgraded from Biodegradable Polymers, Analogous to Petroleum-Derived Polymers, and Newly Developed. *Polymers* **2017**, 9 (10), 523.
- (16) Stasinakis, A. S.; Charalambous, P.; Vyrides, I. Dairy wastewater management in EU: Produced amounts, existing legislation, applied treatment processes and future challenges. *Journal of Environmental Management* **2022**, 303, 114152.
- (17) Ling, S.; Kaplan, D. L.; Buehler, M. J. Nanofibrils in nature and materials engineering. *Nature Reviews Materials* **2018**, 3 (4), 18016.
- (18) Al-Rooqi, M. M.; Hassan, M. M.; Moussa, Z.; Obaid, R. J.; Suman, N. H.; Wagner, M. H.; Natto, S. S. A.; Ahmed, S. A. Advancement of chitin and chitosan as promising biomaterials. *Journal of Saudi Chemical Society* **2022**, *26* (6), 101561.
- (19) Bai, L.; Liu, L.; Esquivel, M.; Tardy, B. L.; Huan, S.; Niu, X.; Liu, S.; Yang, G.; Fan, Y.; Rojas, O. J. Nanochitin: Chemistry, Structure, Assembly, and Applications. *Chem. Rev.* **2022**, *122* (13), 11604–11674.
- (20) Ahmad, S. I.; Ahmad, R.; Khan, M. S.; Kant, R.; Shahid, S.; Gautam, L.; Hasan, G. M.; Hassan, M. I. Chitin and its derivatives: Structural properties and biomedical applications. *Int. J. Biol. Macromol.* **2020**, *164*, 526–539.
- (21) Isobe, N.; Kaku, Y.; Okada, S.; Kawada, S.; Tanaka, K.; Fujiwara, Y.; Nakajima, R.; Bissessur, D.; Chen, C. Identification of Chitin Allomorphs in Poorly Crystalline Samples Based on the Complexation with Ethylenediamine. *Biomacromolecules* **2022**, *23* (10), 4220–4229.
- (22) Amiri, H.; Aghbashlo, M.; Sharma, M.; Gaffey, J.; Manning, L.; Moosavi Basri, S. M.; Kennedy, J. F.; Gupta, V. K.; Tabatabaei, M. Chitin and chitosan derived from crustacean waste valorization streams can support food systems and the UN Sustainable Development Goals. *Nature Food* **2022**, *3* (10), 822–828.
- (23) Vidal, J. L.; Jin, T.; Lam, E.; Kerton, F.; Moores, A. Blue is the new green: Valorization of crustacean waste. *Current Research in Green and Sustainable Chemistry* **2022**, *5*, 100330.
- (24) Rashid, H. A.; Jung, H. Y.; Kim, J. K. Enhanced reutilization value of shrimp-shell waste via fed-batch biodegradation with higher production of reducing sugar, antioxidant, and DNA protective compounds. Fisheries and Aquatic Sciences 2018, 21 (1), 33.
- (25) Pei, Y.; Wang, L.; Tang, K.; Kaplan, D. L. Biopolymer Nanoscale Assemblies as Building Blocks for New Materials: A Review. *Adv. Funct. Mater.* **2021**, *31* (15), 2008552.
- (26) Zhang, M.; Li, Y.; Wang, W.; Yang, Y.; Shi, X.; Sun, M.; Hao, Y.; Li, Y. Comparison of physicochemical and rheology properties of Shiitake stipes-derived chitin nanocrystals and nanofibers. *Carbohydr. Polym.* **2020**, 244, 116468.
- (27) Santos, V. P.; Marques, N. S. S.; Maia, P. C. S. V.; Lima, M. A. B. d.; Franco, L. d. O.; Campos-Takaki, G. M. d. Seafood Waste as Attractive Source of Chitin and Chitosan Production and Their Applications. *International Journal of Molecular Sciences* **2020**, *21* (12), 4290.
- (28) Tsutsumi, Y.; Koga, H.; Qi, Z.-D.; Saito, T.; Isogai, A. Nanofibrillar Chitin Aerogels as Renewable Base Catalysts. *Biomacro-molecules* **2014**, *15* (11), 4314–4319.
- (29) Alavi, F.; Ciftci, O. N. Superlight macroporous aerogels produced from cold-set egg white protein hydrogels show superior oil structuring capacity. *Food Hydrocolloids* **2023**, *136*, 108180.
- (30) Nita, L. E.; Ghilan, A.; Rusu, A. G.; Neamtu, I.; Chiriac, A. P. New Trends in Bio-Based Aerogels. *Pharmaceutics* **2020**, *12* (5), 449.

- (31) Fleury, B.; Abraham, E.; De La Cruz, J. A.; Chandrasekar, V. S.; Senyuk, B.; Liu, Q.; Cherpak, V.; Park, S.; ten Hove, J. B.; Smalyukh, I. I. Aerogel from Sustainably Grown Bacterial Cellulose Pellicles as a Thermally Insulative Film for Building Envelopes. *ACS Appl. Mater. Interfaces* **2020**, *12* (30), 34115–34121.
- (32) Gao, K.; Guo, Y.; Niu, Q.; Fang, H.; Zhang, L.; Zhang, Y.; Wang, L.; Zhou, L. Effects of chitin nanofibers on the microstructure and properties of cellulose nanofibers/chitin nanofibers composite aerogels. *Cellulose* **2018**, 25 (8), 4591–4602.
- (33) Suenaga, S.; Osada, M. Preparation of β -chitin nanofiber aerogels by lyophilization. *Int. J. Biol. Macromol.* **2019**, 126, 1145–1149.
- (34) Zhao, P.; Xie, Y.; Hu, S.; Li, Y.; Xue, X.; Sun, N.; Hu, T.; Zhang, S.; Wang, L. Flexible and Transparent Bagasse Aerogels for Thermal Regulation Glazing. ACS Sustainable Chem. Eng. 2023, 11 (26), 9711–9720.
- (35) Peydayesh, M.; Suter, M. K.; Bolisetty, S.; Boulos, S.; Handschin, S.; Nyström, L.; Mezzenga, R. Amyloid Fibrils Aerogel for Sustainable Removal of Organic Contaminants from Water. *Adv. Mater.* **2020**, 32 (12), 1907932.
- (36) Li, Y.; Liu, Q.; Hess, A. J.; Mi, S.; Liu, X.; Chen, Z.; Xie, Y.; Smalyukh, I. I. Programmable Ultralight Magnets via Orientational Arrangement of Ferromagnetic Nanoparticles within Aerogel Hosts. *ACS Nano* **2019**, *13* (12), 13875–13883.
- (37) Ieamviteevanich, P.; Palaporn, D.; Chanlek, N.; Poo-arporn, Y.; Mongkolthanaruk, W.; Eichhorn, S. J.; Pinitsoontorn, S. Carbon Nanofiber Aerogel/Magnetic Core-Shell Nanoparticle Composites as Recyclable Oil Sorbents. ACS Applied Nano Materials 2020, 3 (4), 3939–3950.
- (38) Jin, J.; Hassanzadeh, P.; Perotto, G.; Sun, W.; Brenckle, M. A.; Kaplan, D.; Omenetto, F. G.; Rolandi, M. A Biomimetic Composite from Solution Self-Assembly of Chitin Nanofibers in a Silk Fibroin Matrix. *Adv. Mater.* **2013**, *25* (32), 4482–4487.
- (39) Shah, N.; Rehan, T.; Li, X.; Tetik, H.; Yang, G.; Zhao, K.; Lin, D. Magnetic aerogel: an advanced material of high importance. *RSC Adv.* **2021**, *11* (13), 7187–7204.
- (40) Wei, G.; Zhang, J.; Usuelli, M.; Zhang, X.; Liu, B.; Mezzenga, R. Biomass vs inorganic and plastic-based aerogels: Structural design, functional tailoring, resource-efficient applications and sustainability analysis. *Prog. Mater. Sci.* 2022, 125, 100915.
- (41) Yang, K.; Zhou, Y.; Wang, Z.; Li, M.; Shi, D.; Wang, X.; Jiang, T.; Zhang, Q.; Ding, B.; You, J. Pseudosolvent Intercalator of Chitin: Self-Exfoliating into Sub-1 nm Thick Nanofibrils for Multifunctional Chitinous Materials. *Adv. Mater.* **2021**, 33 (10), 2007596.
- (42) Jung, J.-M.; Savin, G.; Pouzot, M.; Schmitt, C.; Mezzenga, R. Structure of Heat-Induced β -Lactoglobulin Aggregates and their Complexes with Sodium-Dodecyl Sulfate. *Biomacromolecules* **2008**, 9 (9), 2477–2486.
- (43) Salaberria, A. M.; Diaz, R. H.; Labidi, J.; Fernandes, S. C. M. Role of chitin nanocrystals and nanofibers on physical, mechanical and functional properties in thermoplastic starch films. *Food Hydrocolloids* **2015**, *46*, 93–102.
- (44) Adamcik, J.; Mezzenga, R. Study of amyloid fibrils via atomic force microscopy. *Curr. Opin. Colloid Interface Sci.* **2012**, 17 (6), 369–376.
- (45) Peydayesh, M.; Kistler, S.; Zhou, J.; Lutz-Bueno, V.; Victorelli, F. D.; Meneguin, A. B.; Spósito, L.; Bauab, T. M.; Chorilli, M.; Mezzenga, R. Amyloid-polysaccharide interfacial coacervates as therapeutic materials. *Nat. Commun.* **2023**, *14* (1), 1848.
- (46) Pang, K.; Ding, B.; Liu, X.; Wu, H.; Duan, Y.; Zhang, J. High-yield preparation of a zwitterionically charged chitin nanofiber and its application in a doubly pH-responsive Pickering emulsion. *Green Chem.* **2017**, *19* (15), 3665–3670.
- (47) Usuelli, M.; Germerdonk, T.; Cao, Y.; Peydayesh, M.; Bagnani, M.; Handschin, S.; Nyström, G.; Mezzenga, R. Polysaccharidereinforced amyloid fibril hydrogels and aerogels. *Nanoscale* **2021**, *13* (29), 12534–12545.
- (48) Kang, Y. S.; Risbud, S.; Rabolt, J. F.; Stroeve, P. Synthesis and Characterization of Nanometer-Size Fe3O4 and γ -Fe2O3 Particles. *Chem. Mater.* **1996**, 8 (9), 2209–2211.

- (49) Nguyen, M. D.; Tran, H.-V.; Xu, S.; Lee, T. R. Fe3O4 Nanoparticles: Structures, Synthesis, Magnetic Properties, Surface Functionalization, and Emerging Applications. *Applied Sciences* **2021**, *11* (23), 11301.
- (50) Liao, J.; Huang, H. Magnetic chitin hydrogels prepared from Hericium erinaceus residues with tunable characteristics: A novel biosorbent for Cu2+ removal. *Carbohydr. Polym.* **2019**, 220, 191–201.
- (51) Zou, H.; Lin, B.; Xu, C.; Lin, M.; Zhan, W. Preparation and characterization of individual chitin nanofibers with high stability from chitin gels by low-intensity ultrasonication for antibacterial finishing. *Cellulose* **2018**, 25 (2), 999–1010.
- (52) Peydayesh, M.; Chen, X.; Vogt, J.; Donat, F.; Müller, C. R.; Mezzenga, R. Amyloid fibril-UiO-66-NH2 aerogels for environmental remediation. *Chem. Commun.* **2022**, *58* (33), 5104–5107.
- (53) Hu, B.-C.; Zhang, H.-R.; Li, S.-C.; Chen, W.-S.; Wu, Z.-Y.; Liang, H.-W.; Yu, H.-P.; Yu, S.-H. Robust Carbonaceous Nanofiber Aerogels from All Biomass Precursors. *Adv. Funct. Mater.* **2023**, 33 (1), 2207532.
- (54) Falini, G.; Weiner, S.; Addadi, L. Chitin-Silk Fibroin Interactions: Relevance to Calcium Carbonate Formation in Invertebrates. *Calcified Tissue International* **2003**, 72 (5), 548–554.
- (55) Liao, J.; Huang, H. Preparation, Characterization and Gelation of a Fungal Nano Chitin Derived from Hericium erinaceus Residue. *Polymers* **2022**, *14* (3), 474.
- (56) Li, G.-y.; Jiang, Y.-r.; Huang, K.-l.; Ding, P.; Chen, J. Preparation and properties of magnetic Fe3O4-chitosan nanoparticles. *J. Alloys Compd.* **2008**, 466 (1), 451–456.
- (57) Peydayesh, M.; Greber, T.; Haechler, I.; Armanious, A.; Jia, X.; Usuelli, M.; Bagnani, M.; Mezzenga, R. Renewable Water Harvesting by Amyloid Aerogels and Sun. *Advanced Sustainable Systems* **2022**, *6* (1), 2100309 (accessed Nov 2, 2023).
- (58) Liu, L.; Bai, L.; Tripathi, A.; Yu, J.; Wang, Z.; Borghei, M.; Fan, Y.; Rojas, O. J. High Axial Ratio Nanochitins for Ultrastrong and Shape-Recoverable Hydrogels and Cryogels via Ice Templating. *ACS Nano* **2019**, *13* (3), 2927–2935.
- (59) Zhang, Y.; Yang, B.; Zhang, X.; Xu, L.; Tao, L.; Li, S.; Wei, Y. A magnetic self-healing hydrogel. *Chem. Commun.* **2012**, 48 (74), 9305–9307.
- (60) Ding, B.; Zhao, D.; Song, J.; Gao, H.; Xu, D.; Xu, M.; Cao, X.; Zhang, L.; Cai, J. Light weight, mechanically strong and biocompatible α -chitin aerogels from different aqueous alkali hydroxide/urea solutions. *Science China Chemistry* **2016**, *59* (11), 1405–1414.
- (61) Wei, J.; Yang, Z.; Sun, Y.; Wang, C.; Fan, J.; Kang, G.; Zhang, R.; Dong, X.; Li, Y. Nanocellulose-based magnetic hybrid aerogel for adsorption of heavy metal ions from water. *J. Mater. Sci.* **2019**, *54* (8), 6709–6718.
- (62) ALOthman, Z. A. A Review: Fundamental Aspects of Silicate Mesoporous Materials. *Materials* **2012**, *5* (12), 2874–2902.
- (63) Maleki, H.; Durães, L.; Costa, B. F. O.; Santos, R. F.; Portugal, A. Design of multifunctional magnetic hybrid silica aerogels with improved properties. *Microporous Mesoporous Mater.* **2016**, 232, 227–237.
- (64) Hou, J.; Aydemir, B. E.; Dumanli, A. G. Understanding the structural diversity of chitins as a versatile biomaterial. *Philosophical Transactions of the Royal Society A: Mathematical, Physical and Engineering Sciences* **2021**, 379 (2206), 20200331.
- (65) Bianco, L. D.; Lesci, I. G.; Fracasso, G.; Barucca, G.; Spizzo, F.; Tamisari, M.; Scotti, R.; Ciocca, L. Synthesis of nanogranular Fe3O4/biomimetic hydroxyapatite for potential applications in nanomedicine: structural and magnetic characterization. *Materials Research Express* **2015**, 2 (6), 065002.
- (66) Dormann, J. L.; Fiorani, D.; Tronc, E. Magnetic Relaxation in Fine-Particle Systems. *Advances in Chemical Physics* **1997**, 98, 283–494.
- (67) Chantrell, R. W.; O'Grady, K. The Magnetic Properties of Fine Particles. In *Applied Magnetism*; Gerber, R., Wright, C. D., Asti, G., Eds.; Springer Netherlands, 1994; pp 113–164.
- (68) Royer, S.; Duprez, D. Catalytic Oxidation of Carbon Monoxide over Transition Metal Oxides. *ChemCatChem* **2011**, 3 (1), 24–65.
- (69) Schubert, M. M.; Hackenberg, S.; van Veen, A. C.; Muhler, M.; Plzak, V.; Behm, R. J. CO Oxidation over Supported Gold Catalysts—

- "Inert" and "Active" Support Materials and Their Role for the Oxygen Supply during Reaction. J. Catal. 2001, 197 (1), 113–122.
- (70) Daniells, S. T.; Overweg, A. R.; Makkee, M.; Moulijn, J. A. The mechanism of low-temperature CO oxidation with Au/Fe2O3 catalysts: a combined Mössbauer, FT-IR, and TAP reactor study. *J. Catal.* **2005**, 230 (1), 52–65.
- (71) Jiang, X. C.; Yu, A. B. Synthesis of Pd/ α -Fe2O3 nanocomposites for catalytic CO oxidation. *Journal of Materials Processing Technology* **2009**, 209 (9), 4558–4562.
- (72) Han, Q.; Zhang, D.; Guo, J.; Zhu, B.; Huang, W.; Zhang, S. Improved Catalytic Performance of Au/α-Fe2O3-Like-Worm Catalyst for Low Temperature CO Oxidation. *Nanomaterials* **2019**, *9* (8), 1118.
- (73) Akita, T.; Maeda, Y.; Kohyama, M. Low-temperature CO oxidation properties and TEM/STEM observation of Au/ γ -Fe2O3 catalysts. *J. Catal.* **2015**, 324, 127–132.
- (74) Kwon, S. C.; Fan, M.; Wheelock, T. D.; Saha, B. Nano- and micro-iron oxide catalysts for controlling the emission of carbon monoxide and methane. *Sep. Purif. Technol.* **2007**, *58* (1), 40–48.
- (75) Abdel Halim, K. S.; Khedr, M. H.; Nasr, M. I.; El-Mansy, A. M. Factors affecting CO oxidation over nanosized Fe2O3. *Mater. Res. Bull.* **2007**, 42 (4), 731–741.
- (76) Li, P.; Miser, D. E.; Rabiei, S.; Yadav, R. T.; Hajaligol, M. R. The removal of carbon monoxide by iron oxide nanoparticles. *Applied Catalysis B: Environmental* **2003**, 43 (2), 151–162.
- (77) Zhao, K.; Tang, H.; Qiao, B.; Li, L.; Wang, J. High Activity of Au/ γ -Fe2O3 for CO Oxidation: Effect of Support Crystal Phase in Catalyst Design. *ACS Catal.* **2015**, *5* (6), 3528–3539.
- (78) Wang, L.; Pu, C.; Xu, L.; Cai, Y.; Guo, Y.; Guo, Y.; Lu, G. Effect of supports over Pd/Fe2O3 on CO oxidation at low temperature. *Fuel Process. Technol.* **2017**, *160*, 152–157.
- (79) Gallagher, K. J.; Feitknecht, W.; Mannweiler, U. Mechanism of Oxidation of Magnetite to γ -Fe2O3. *Nature* **1968**, 217 (5134), 1118–1121.
- (80) El Mendili, Y.; Bardeau, J.-F.; Randrianantoandro, N.; Grasset, F.; Greneche, J.-M. Insights into the Mechanism Related to the Phase Transition from γ -Fe2O3 to α -Fe2O3 Nanoparticles Induced by Thermal Treatment and Laser Irradiation. *J. Phys. Chem. C* **2012**, *116* (44), 23785–23792.
- (81) Zhang, X.; Han, D.; Hua, Z.; Yang, S. Porous Fe3O4 and gamma-Fe2O3 foams synthesized in air by sol-gel autocombustion. *J. Alloys Compd.* **2016**, *684*, 120–124.
- (82) Özdemir, Ö.; Banerjee, S. K. High temperature stability of maghemite (γ -Fe2O3). *Geophys. Res. Lett.* **1984**, 11 (3), 161–164.
- (83) Bolisetty, S.; Vallooran, J. J.; Adamcik, J.; Handschin, S.; Gramm, F.; Mezzenga, R. Amyloid-mediated synthesis of giant, fluorescent, gold single crystals and their hybrid sandwiched composites driven by liquid crystalline interactions. *J. Colloid Interface Sci.* **2011**, 361 (1), 90–96.
- (84) Bagnani, M.; Nyström, G.; De Michele, C.; Mezzenga, R. Amyloid Fibrils Length Controls Shape and Structure of Nematic and Cholesteric Tactoids. *ACS Nano* **2019**, *13* (1), 591–600.
- (85) Seoudi, R.; Nada, A. M. A. Molecular structure and dielectric properties studies of chitin and its treated by acid, base and hypochlorite. *Carbohydr. Polym.* **2007**, *68* (4), 728–733.
- (86) You, J.; Zhu, L.; Wang, Z.; Zong, L.; Li, M.; Wu, X.; Li, C. Liquid exfoliated chitin nanofibrils for re-dispersibility and hybridization of two-dimensional nanomaterials. *Chemical Engineering Journal* **2018**, 344, 498–505.
- (87) Wang, J.; Chen, Z.; Naguib, H. E. Preparation of a novel double crosslinked chitin aerogel via etherification with high strength. *Carbohydr. Polym.* **2021**, 265, 118014.
- (88) Heath, L.; Zhu, L.; Thielemans, W. Chitin Nanowhisker Aerogels. ChemSusChem 2013, 6 (3), 537–544.